



# A simple model catalyst study to distinguish the roles of different oxygen species in propane and soot combustion

Xuezan Mao<sup>a,1</sup>, Shuran Liu<sup>b,1</sup>, Wei Liu<sup>a</sup>, Xiaodong Wu<sup>b,\*</sup>, Shuang Liu<sup>a,\*</sup>

<sup>a</sup> School of Materials Science and Engineering, Ocean University of China, Qingdao 266100, China

<sup>b</sup> Key Laboratory of Advanced Materials of Ministry of Education of China, School of Materials Science and Engineering, Tsinghua University, Beijing 100084, China

## ARTICLE INFO

### Keywords:

CeO<sub>2</sub>  
Pr<sub>6</sub>O<sub>11</sub>  
Propane and soot combustion  
O<sub>x</sub><sup>n</sup> species  
Lattice oxygen

## ABSTRACT

It is important yet difficult to distinguish the specific roles of superficial O<sub>x</sub><sup>n</sup> and interfacial lattice oxygen in catalytic combustion, especially over catalysts consisting of reducible metal oxides. In this study, based on the comparison of two natural counterparts with similar structure — CeO<sub>2</sub> (an O<sub>x</sub><sup>n</sup> generator) and Pr<sub>6</sub>O<sub>11</sub> (a lattice oxygen contributor), it is suggested that the catalytic combustion of propane under lean-burn conditions followed a typical Mars-van Krevelen mechanism, in which catalyst lattice oxygen represented the dominant reactive phases while superficial O<sub>x</sub><sup>n</sup> played negligible roles. As for soot combustion, adsorbed O<sub>x</sub><sup>n</sup> represented more sustainable oxidants than lattice oxygen (drained easily at the beginning of the reactions). Such a comparison is readily achieved and widely applicable, which may shed light on the identification of dominant reactive phases for various oxidation reactions over oxide-based catalysts.

## 1. Introduction

Oxygen plays an essential role in catalysis. It is not only a component of the most widely used type of catalysts — oxides, but also the reactant of one of the most important types of catalytic reactions — oxidation [1]. In spite of the mass of results reported so far, there has been a lot of uncertainty in the key oxidant in catalytic (deep) oxidation over reducible metal oxides (e.g., ceria [2]). For instance, it is plausible to assume the combustion of alkanes on ceria follows the Mars-van Krevelen (redox) catalytic cycles, in which the (kinetically relevant) reduction part involves the abstraction of hydrogen from alkanes by vicinal lattice oxygen atoms (O<sup>2-</sup>), giving rise to hydroxyls and thereby oxygen vacancies upon the re-combinative desorption of H<sub>2</sub>O [3,4]. In the re-oxidation part of the redox cycles, the consumed ceria lattice oxygen is restored, accompanying by the formation of O<sub>2</sub>-derived adsorbed intermediates (e.g., superoxide, peroxide) at the Ce<sup>3+</sup>-V<sub>O</sub> structure [5,6]. Due to the high hydrogen affinity of these electrophilic O<sub>x</sub><sup>n</sup> species [7–10], they were reportedly stronger alkane igniters than the nucleophilic lattice O<sup>2-</sup> [1,11]. Nevertheless, because of the entanglement of these ceria interfacial and superficial oxygen species, the distinguishing of their specific roles in alkane combustion has not been unambiguously achieved [12–14], let alone the proposing of a general

theory for alkane catalytic combustion over different reducible metal oxides.

Similar to the case of alkanes, the principal oxidizing agents in the ceria-assisted combustion of soot — a more complex carbon-containing reactant than alkanes — remain elusive. Bueno-López et al. were among the earliest exploring soot combustion over ceria with isotopic labeled oxygen, and concluded that such reactions follow a typical Mars-van Krevelen mechanism [15,16]. Their conclusions were consistent with the ETEM data obtained by Simonsen et al. [17], in which the elimination of soot happened only at the ceria-soot contact points. However, the later study of both Krishna et al. [18] and Machida et al. [19] highlighted the involvement of adsorbed O<sub>x</sub><sup>n</sup> in these reactions, which was further confirmed by the groups of Yamazaki [20,21], Llorca [22, 23] and us [24,25]. Specifically, the electrophilic oxygen species may attack the carbon rings (from their central part) and break the graphite layers [26]. The thus-generated nanotunnels allow direct oxidation of the amorphous carbon cores — which are more vulnerable than the graphite layers — and lead to the destruction of soot particles from inside [27]. In spite of these findings, the contribution of O<sub>x</sub><sup>n</sup> to soot combustion is much less straightforward than that of ceria lattice oxygen. After generating at the Ce<sup>3+</sup>-V<sub>O</sub> structure, the O<sub>x</sub><sup>n</sup> species may have to travel across some distance before reacting with soot [18], and their

\* Corresponding authors.

E-mail addresses: [wuxiaodong@tsinghua.edu.cn](mailto:wuxiaodong@tsinghua.edu.cn) (X. Wu), [lius@ouc.edu.cn](mailto:lius@ouc.edu.cn) (S. Liu).

<sup>1</sup> These two authors contributed equally to this work.

efficiency is therefore strongly affected by the  $V_O$ -trapping ( $O_x^- + V_O \rightarrow V_O-O_x^-$ ) and  $O_x^-$  annihilation ( $O_x^- \rightarrow O^{2-}$ ) effects caused by ceria [25,28].

Isotopic tracer studies have been proven powerful techniques for elucidating the dominant oxidants in combustion reactions over reducible oxides [19,29]. However, since the ceria interfacial  $\leftrightarrow$  superficial and bulk  $\leftrightarrow$  surface oxygen exchange proceed very fast at the typical combustion temperatures of alkanes and soot (i.e.,  $\geq 300^\circ\text{C}$ ) [30], it is usually difficult to make such elucidation without building comprehensive kinetic/molecular models in advance [31,32]. Herein, we propose a simple strategy to circumvent the entanglement of different oxygen species via comparing ceria with praseodymia.  $\text{CeO}_2$  and  $\text{Pr}_6\text{O}_{11}$  share identical cubic fluorite-like structure, based on which they form a multitude of  $\text{CeO}_{2-x}$  and  $\text{PrO}_x$  phases due to the reduction of the oxygen content by the formation of oxygen vacancies in the lattice [33]. Importantly, as a result of the considerably smaller electrochemical reduction potential of  $\text{Ce}^{4+}/\text{Ce}^{3+}$  (1.74 eV) than that of  $\text{Pr}^{4+}/\text{Pr}^{3+}$  (3.2 eV), Ce and Pr prefer the +4 and +3 valences in these oxides, respectively, which leads to the easier reduction (i.e., lattice oxygen utilization [34]) but more difficult re-oxidation (i.e.,  $O_x^-$  formation [19]) of  $\text{Pr}_6\text{O}_{11}$  in comparison with  $\text{CeO}_2$ . In this work, the catalytic combustion of propane (an alkane with sufficient representative geometry [35]) and Printex-U (a classic substitute of the diesel soot [18]) were investigated over rod-like  $\text{Pr}_6\text{O}_{11}$  and  $\text{CeO}_2$  under lean-burn conditions. Distinct dependence on the types of reactive oxygen was observed for these two carbon-containing reactants. Such a study may shed light on the identification of key reactive phases over catalysts consisting of reducible metal oxides.

## 2. Experimental section

### 2.1. Catalyst synthesis

$\text{CeO}_2$  and  $\text{Pr}_6\text{O}_{11}$  nanorods were prepared via similar hydrothermal methods. In a typical synthesis,  $\text{CeCl}_3 \cdot 7\text{H}_2\text{O}$  (5 mmol, Aladdin, 99.9%) or  $\text{Pr}(\text{NO}_3)_3 \cdot 6\text{H}_2\text{O}$  (0.2 mol, Aladdin, 99.9%) was dissolved in (40 or 20 mL of) deionized water. Afterwards, (30 or 20 mL of) NaOH (Macklin, 96%) aqueous solution was added dropwise under vigorous stirring. The mixtures were stirred for an additional 0.5 h, transferred into a (100 or 50 mL) Teflon-lined stainless steel autoclave, and hydrothermally treated at  $130^\circ\text{C}$  for 5 h ( $\text{CeO}_2$ ) or at  $120^\circ\text{C}$  for 45 h ( $\text{Pr}_6\text{O}_{11}$ ). The filtrated precipitates were washed with water and ethanol repeatedly until the filtered solution was chlorine-free (confirmed by adding  $\text{AgNO}_3$  solution), dried at  $80^\circ\text{C}$  overnight and calcined at  $600^\circ\text{C}$  for 2 h in static air to obtain the  $\text{CeO}_2$  and  $\text{Pr}_6\text{O}_{11}$  nanorods. As shown in Table S1, the impurity contents over the sample were low and could thereby be ignored.

### 2.2. General characterizations

**Prior to each of the following characterizations, the samples were pretreated in static air at  $500^\circ\text{C}$  for 30 min to exclude the interference of adsorbed carbonates.**

The solid properties of the catalysts were obtained via transmission electron microscopy (JEOL 2100 with an accelerating voltage of 200 kV and a point resolution of 0.19 nm), powder X-ray diffraction patterns (D8 ADVANCE employing Cu-K $\alpha$  radiation), and  $\text{N}_2$  physisorption experiments at  $-196^\circ\text{C}$  (JW-BK200C). The specific surface areas of the catalyst were calculated by the Brunauer-Emmett-Teller (BET) method.

The acid and base properties of the catalysts were studied by pyridine adsorption infrared spectroscopy (Py-IR) and  $\text{CO}_2$  temperature-programmed desorption ( $\text{CO}_2$ -TPD), respectively. In a typical Py-IR test, the catalysts were placed in a Fourier transform spectrometer (Perkin Elmer model Spectrum 100) and outgassed at  $350^\circ\text{C}$  for 2 h. IR spectra were recorded at room temperature, after admission of pyridine, adsorption at room temperature and evacuation at 200 or  $350^\circ\text{C}$ . In a typical  $\text{CO}_2$ -TPD test, 100 mg of catalysts were exposed to 1%  $\text{CO}_2/\text{N}_2$

(500 mL/min) at  $100^\circ\text{C}$  for 30 min and flushed with  $\text{N}_2$  (500 mL/min) for another 30 min. Then the  $\text{CO}_2$  desorption profiles (analyzed using an infrared spectrometer (MKS Multigas 6030)) were obtained by heating the reactor at  $5^\circ\text{C}/\text{min}$  in  $\text{N}_2$  (500 mL/min).

The presence and generation of defects on the catalysts were verified by electron paramagnetic resonance (EPR) as well as X-ray photoelectron spectra (XPS). These spectra were recorded on an X-band Eleksys 500 EPR spectrometer (90 K, Bruker) and an ESCALAB 250 Xi system equipped with monochromatic Al K $\alpha$  (1486.6 eV) X-ray source, respectively.

### 2.3. Specific characterizations

**Prior to each of the following characterizations, the samples were pretreated in static air at  $500^\circ\text{C}$  for 30 min to exclude the interference of adsorbed carbonates.**

$\text{O}_2$  temperature-programmed desorption ( $\text{O}_2$ -TPD) was performed to quantify the total active oxygen species that released from the catalysts. The tests were carried out in a vertical fixed-bed quartz reactor. For each test, 100 mg of catalyst was placed in a quartz tube and heated up to  $600^\circ\text{C}$  ( $5^\circ\text{C}/\text{min}$ ) in  $\text{N}_2$  (500 mL/min).  $\text{O}_2$  generated during the heating process was monitored as ion current signals by a mass spectrometer (MS, OmniStar 200).

Propane temperature-programmed reduction ( $\text{C}_3\text{H}_8$ -TPR) was performed to quantify the active oxygen species of the catalysts that accessible for propane. The tests were carried out in a vertical fixed-bed quartz reactor. For each test, 100 mg of catalyst was placed in a quartz tube and heated up to  $600^\circ\text{C}$  ( $5^\circ\text{C}/\text{min}$ ) in 800 ppm  $\text{C}_3\text{H}_8/\text{N}_2$  (50 mL/min).  $\text{CO}_x$  ( $\text{CO}$  and  $\text{CO}_2$ ) generated was analyzed using an infrared spectrometer (MKS Multigas 6030).

Soot temperature-programmed reduction (soot-TPR) was performed to quantify the active oxygen species of the catalysts that accessible for soot. The tests were carried out in a vertical fixed-bed quartz reactor. For each test, 100 mg of catalyst and 10 mg of soot (Printex-U, diameter 25 nm, surface area  $100\text{ m}^2/\text{g}$ , Degussa) were mixed and ground in an agate mortar for 5 min, which were then placed in a quartz tube and heated up to  $600^\circ\text{C}$  ( $5^\circ\text{C}/\text{min}$ ) in  $\text{N}_2$  (50 mL/min).  $\text{CO}_x$  ( $\text{CO}$  and  $\text{CO}_2$ ) generated during the heating process was analyzed using an infrared spectrometer (MKS Multigas 6030). Notably, no  $\text{CO}_x$  production was detected when heating the model soot alone in  $\text{N}_2$ .

To verify the activation of propane on catalyst surface, diffuse reflectance infrared Fourier transform (DRIFT) spectra were measured on a FT-IR spectrometer (Thermo Nicolet 6700) using a heatable environmental reaction cell with ZnSe windows, which was connected to a gas-dosing system. For each test, spectra were collected under  $\text{N}_2$  at specified temperatures and used as the background. A gas flow containing 800 ppm  $\text{C}_3\text{H}_8/\text{N}_2$  or 800 ppm  $\text{C}_3\text{H}_8/5\%\text{ O}_2/\text{N}_2$  (100 mL/min) was introduced and held for 30 min. Then the atmosphere was switched to  $\text{N}_2$  (100 mL/min) and held for another 30 min, after which the IR spectra were recorded.

### 2.4. Activity measurements

**Prior to each of the following activity tests, the samples were pretreated in static air at  $500^\circ\text{C}$  for 30 min to exclude the interference of adsorbed carbonates.**

Temperature-programmed oxidation (TPO) tests were performed to estimate the activity sequence of the catalysts. The tests were carried out in a vertical fixed-bed quartz reactor with the effluent gases monitored by an infrared spectrometer (MKS Multigas 6030). During the  $\text{C}_3\text{H}_8$ -TPO tests, 100 mg of catalysts (40–60 mesh) were diluted with 300 mg silica pellets (40–60 mesh) to minimize the influence of hot spots. For the soot-TPO tests, 100 mg of catalysts and 10 mg of Printex-U were ground in an agate mortar for 5 min, sieved to 40–60 mesh before mixing with the silica pellets. The “tight” catalyst-soot contact mode was used to establish good reproducibility of the experiments and to evaluate the intrinsic

kinetic parameters [18,36]. The mixtures were placed in a quartz tube and heated up to 600°C (5°C/min) in simulated lean-burn diesel exhausts: 800 ppm C<sub>3</sub>H<sub>8</sub>/5% O<sub>2</sub>/N<sub>2</sub> with/without 5 vol% H<sub>2</sub>O (500 mL/min, GHSV = 100,000 h<sup>-1</sup>) or 5% O<sub>2</sub>/N<sub>2</sub> with/without 5 vol% H<sub>2</sub>O (500 mL/min, GHSV = 100,000 h<sup>-1</sup>). The apparent activation energy ( $E_a^{\text{app}}$ ) of soot combustion was measured according to the Ozawa method on the basis of soot-TPO tests with different heating rates ( $\beta = 1, 2, 5$  and 10 °C/min). The expression “ $\log(\beta) = B - 0.4567E_a/(RT_{50})$ ” was applied, where  $B$  is a constant value,  $R$  is the universal gas constant and  $E_a$  is the apparent activation energy.  $T_{50}$  is the temperature corresponding to 50% soot conversion in the soot-TPO tests. Estimates of  $E_a^{\text{app}}$  can be calculated from the slope of the best-fitting line of the  $\log(\beta)$  versus  $1/T_{50}$  data series.

Isothermal reactions were carried out in the same apparatus and atmosphere used in the TPO runs to quantify the catalysts' intrinsic activity. These tests were performed at temperatures which ensured < 10% propane and soot conversions (to guarantee they worked in the kinetic regime and prevent significant soot removal from the sample). The apparent activation energy ( $E_a^{\text{app}}$ ) and pre-exponential factor  $A$  of propane combustion were obtained based on the steady-state results by plotting the  $\ln(r_{\text{C}_3\text{H}_8})$  values as a function of  $1/T$  via an Arrhenius-type function ( $r_{\text{C}_3\text{H}_8} = Ae^{-E_a/RT}$ ).  $E_a$  and the pre-exponential factors ( $A$ ) were obtained from the slope of the fitted linear plots and the ordinate values at  $1/T = 0$ , respectively.

### 3. Results and discussion

#### 3.1. Solid properties

Morphologies of the catalysts are illustrated in Fig. 1a–1c. Both the CeO<sub>2</sub> and Pr<sub>6</sub>O<sub>11</sub> samples exhibited typical cubic fluorite structure and rod-like morphologies with widths and lengths varying in the range of 5–25 and 40–240 nm, respectively. The similarity in morphologies allowed these catalysts to contact with soot in similar manners, which is a crucial factor in comparing their intrinsic soot combustion activity (see Fig. S1 for details) [25,36]. Due to the relatively high calcination temperature (600°C) during synthesis, most of the CeO<sub>2</sub> and Pr<sub>6</sub>O<sub>11</sub> nanorods were enclosed by their thermally stable {111} facets [24]. As shown in Fig. 1d, in spite of the higher BET surface area of CeO<sub>2</sub> (63 m<sup>2</sup>/g) than Pr<sub>6</sub>O<sub>11</sub> (40 m<sup>2</sup>/g), both the samples showed identical type IV adsorption-desorption isotherm with H3 hysteresis loop.

The acid/base properties of the oxides were investigated by Py-IR and CO<sub>2</sub>-TPD, which are potential contributing factors for the catalytic combustion of propane (via boosted heterolytic C-H bond cleavage over strong Lewis acid-base pairs [37,38]) and soot (via accelerated formation and decomposition of surface oxygen complexes induced by strong acid sites [39,40]). As shown in Fig. 1e, the pyridinium ion (PyH<sup>+</sup>) on Brønsted acid sites and the coordinatively bound pyridine on Lewis acid sites (Ce<sup>x+</sup> or Pr<sup>x+</sup> unsaturated coordinations) showed bands at around 1545 and 1445 cm<sup>-1</sup>, respectively [41,42]. According to the quantitative data in Table 1, there were about 1.15 times more acid sites over CeO<sub>2</sub> than over Pr<sub>6</sub>O<sub>11</sub>, most of which exhibited relatively weak acidity (especially for the case of Lewis sites). Similarly, both the samples showed no strong basic sites, as they held relatively low amounts of CO<sub>2</sub> (0.09–0.12 mmol CO<sub>2</sub>/g<sub>cat</sub>, Table 1), and no CO<sub>2</sub> was desorbed at temperatures higher than 350 °C during the CO<sub>2</sub>-TPD tests (Fig. 1f) [42]. Based on the Py-IR and CO<sub>2</sub>-TPD results, it is suggested that the (similar weak) acid/base sites on CeO<sub>2</sub> and Pr<sub>6</sub>O<sub>11</sub> could hardly make significant differences in their propane and soot combustion performance [37–40].

#### 3.2. Presence and involvement of different oxygen species

The presence and involvement of superficial/interfacial oxygen species in catalytic reactions were characterized by EPR, O<sub>2</sub>-TPD and C<sub>3</sub>H<sub>8</sub>/soot-TPR tests. As shown in Fig. 2a, the EPR signals of Ce<sup>3+</sup> cations could be clearly observed over CeO<sub>2</sub>, accompanying by a distinct peak at

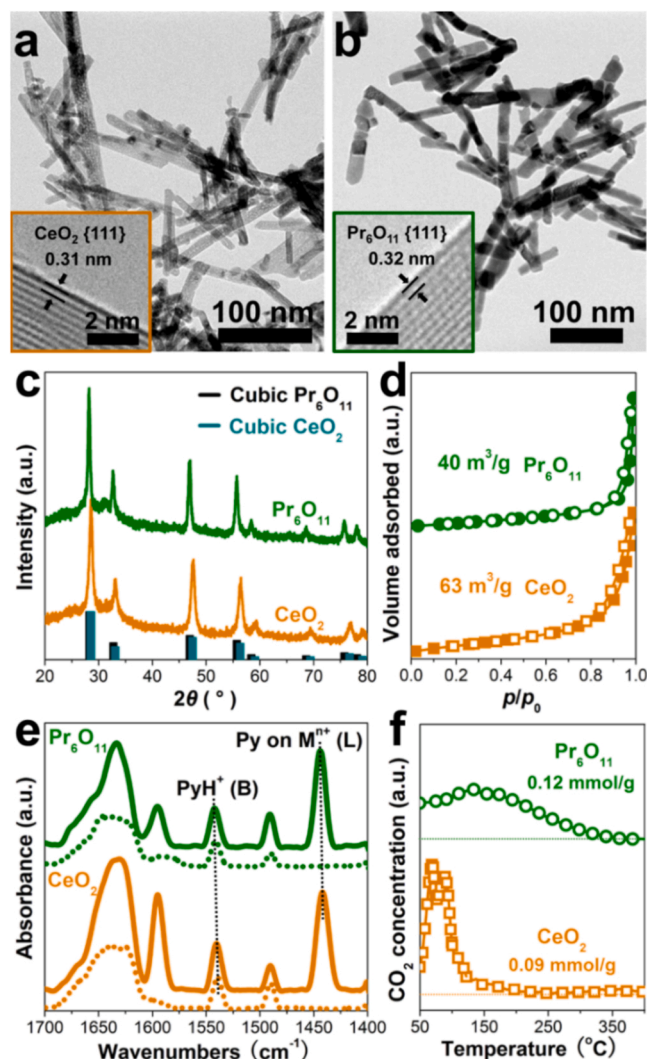


Fig. 1. Typical HRTEM images of the rod-like (a) CeO<sub>2</sub> and (b) Pr<sub>6</sub>O<sub>11</sub>, their (c) XRD patterns, (d) N<sub>2</sub> adsorption-desorption isotherms (solid: adsorption, open: desorption), (e) pyridine (Py) adsorption IR spectra (solid: evacuation at 200 °C, dot: evacuation at 350 °C) and (f) CO<sub>2</sub>-TPD profiles.

Table 1

Summary of structural properties of the catalysts.

Sample	$S_{\text{BET}}$ (m <sup>2</sup> /g) <sup>a</sup>	Total Brønsted acid sites (mmol/ g) <sup>b</sup>	Total Lewis acid sites (mmol/ g) <sup>b</sup>	Moderate/ strong Brønsted acid sites (mmol/g) <sup>c</sup>	Moderate/ strong Lewis acid sites (mmol/g) <sup>c</sup>	Total basic sites (mmol/ g) <sup>d</sup>
CeO <sub>2</sub>	63	0.023	0.044	0.014	0	0.09
Pr <sub>6</sub> O <sub>11</sub>	40	0.019	0.039	0.011	0	0.12

<sup>a</sup> BET surface area obtained from N<sub>2</sub> physisorption tests at -196°C.

<sup>b</sup> Obtained from the IR spectra of Py adsorption after evacuation at 200°C.

<sup>c</sup> Obtained from the IR spectra of Py adsorption after evacuation at 350°C.

<sup>d</sup> Obtained from the CO<sub>2</sub>-TPD data.

$g = 2.005$  assigning to O<sub>2</sub><sup>-</sup> species bonded to Ce<sup>3+</sup> and located at an associated surface vacancy defect (O<sub>2</sub><sup>-</sup>-Ce<sup>3+</sup>-V<sub>O</sub>) [43]. The presence of O<sub>2</sub><sup>-</sup>, as well as the (diamagnetic and thereby EPR-silent) O<sub>2</sub><sup>2-</sup> species on CeO<sub>2</sub> was further confirmed by O<sub>2</sub>-TPD. These superficial oxygen species gave rise to overlapped O<sub>2</sub> desorption peaks at temperatures below 300 °C (Fig. 2b) [44]. Similar to the results obtained by Machida et al. [19], no O<sub>2</sub><sup>-</sup>-related EPR signals could be detected over Pr<sub>6</sub>O<sub>11</sub>. This



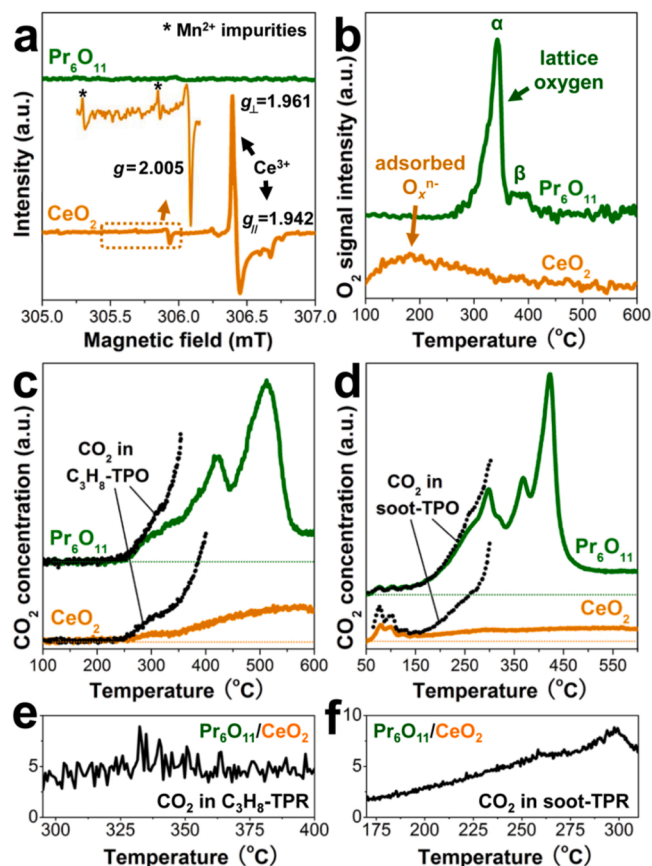


**Fig. 2.** (a) EPR spectra, (b)  $O_2$ -TPD profiles of  $CeO_2$  and  $Pr_6O_{11}$ ,  $CO_2$  produced in the TPR (without  $O_2$ ) and TPO (with  $O_2$ ) tests by using (c) propane and (d) soot as probes, and the ratios of  $Pr_6O_{11}$ - and  $CeO_2$ -induced  $CO_2$  production in the (e)  $C_3H_8$ -TPR and (f) soot-TPR tests.

sample desorbed considerable amount of  $O_2$  at 300–420 °C (the “ $\alpha$ ” and “ $\beta$ ” oxygen peaks) during the  $O_2$ -TPD tests, which should be attributed to the lattice oxygen in praseodymium oxides [45].

From the data in Fig. 2a and 2b, it is clear that as designed, the  $CeO_2$  and  $Pr_6O_{11}$  catalysts preferred the generation/release of adsorbed  $O_x^{n-}$  species and lattice oxygen, respectively. These differences were a consequence of the smaller electrochemical reduction potential of  $Ce^{4+}/Ce^{3+}$  (1.74 eV) than that of  $Pr^{4+}/Pr^{3+}$  (3.2 eV), which led to the preference of +4 and +3 valences for Ce and Pr in the oxides, respectively. As a result, the reduction (lattice oxygen release) of praseodymia (e.g.,  $Pr_6O_{11} \rightarrow Pr_2O_3$ ) is much easier than that of ceria (e.g.,  $CeO_2 \rightarrow Ce_2O_3$ ) (see also the  $H_2$ -TPR results in Fig. S2) [33,34]. Correspondingly, the re-oxidation of  $PrO_x$  — whose key step is the electron transfer between  $Pr^{3+}$  and gaseous  $O_2$  ( $Pr^{3+} + O_2 \rightarrow Pr^{4+} + O_x^{n-}$ ) — goes much more slowly than that of  $CeO_{2-x}$  ( $Ce^{3+} + O_2 \rightarrow Ce^{4+} + O_x^{n-}$ ) [5,6]. Therefore, superficial  $O_x^{n-}$  species were observed on  $CeO_2$  but not on  $Pr_6O_{11}$ .

To investigate the roles of catalyst-derived oxygen species in the reactions, anaerobic propane and soot oxidation (TPR) tests were

performed with results presented in Fig. 2c, 2d and Table 2. In comparison with propane (whose catalytic combustion experiences adsorption and activation processes [3]), soot as a stronger reductant led to obviously deeper reduction (2.3–2.8 times more  $CO_2$  generation) of the catalysts. Due to the high mobility of the lattice oxygen in  $Pr_6O_{11}$  (Fig. 2b), this sample consumed considerably more propane (3.5 times in total, ~5 times at 300–400 °C, see Fig. 2e) and soot (4.3 times in total, 2–9 times at 170–320 °C, see Fig. 2f) than did  $CeO_2$  during the tests. The ignition temperatures for propane and soot maintained constant in the presence/absence of gaseous  $O_2$ , which provided the thermodynamic rationale for the involvement of  $Pr_6O_{11}/CeO_2$  interfacial lattice oxygen (via the Mars-van Krevelen mechanism) in the initial stage of the reactions [31,32].

### 3.3. Activities of the catalysts

Intrinsic activities of the catalysts were investigated by steady-state measurements. As shown in Fig. 3a and Table 3,  $Pr_6O_{11}$  exhibited 5–6 times higher propane combustion rate (normalized by catalyst surface area [11]) than did  $CeO_2$  in the kinetic regime. Such a ratio was close to that of the propane consumed by  $Pr_6O_{11}$  and  $CeO_2$  in the TPR (anaerobic propane oxidation) tests (Fig. 2e), indicating the direct involvement of catalyst lattice oxygen in propane combustion. The performance advantage of  $Pr_6O_{11}$  over  $CeO_2$  extended to the non-kinetic region, resulting in a  $\Delta T_{50}$  of 58 °C in their  $C_3H_8$ -TPO tests (Fig. 3b and Table 3). Furthermore, by examining catalyst activity at different temperatures, the apparent activation energy ( $E_a^{app}$ ) and pre-exponential factor ( $A$ ) of  $CeO_2$  were calculated to be 75 kJ/mol and  $1.1 \times 10^{-3} \text{ mol/m}^2\text{s}^{-1}$ , respectively (Fig. 3c and Table 3). Interestingly, both the  $E_a^{app}$  (82 kJ/mol) and the  $A$  ( $2.4 \times 10^{-2} \text{ mol/m}^2\text{s}^{-1}$ ) of  $Pr_6O_{11}$  were larger than those of  $CeO_2$ . Such relationships resembled the results obtained in methane catalytic combustion [46], which could be rationalized via the compensation effect induced by kinetic regime shift. Specifically, for reactions with effectively bound precursor (e.g. the propane  $\sigma$ -complexes in propane combustion), once including the contribution of the propane adsorption energy ( $\Delta E$ ) and the surface entropic configuration ( $\Delta S$ ),  $Pr_6O_{11}$  with relatively low coverage of the kinetically-relevant intermediates (high  $\theta_*$  values, further evidence shown in Section 3.4) would exhibit high  $E_a^{app}$  that balanced out by enlarged  $A$  values, which ultimately led to its large  $r_{C_3H_8}$  values [47,48].

Water vapor is not only a product of propane combustion, but also a typical component in vehicle exhausts. Therefore, it is essential to understand the role of steam in reaction kinetics and the overall reaction rate. As shown in Fig. 3c, the presence of water led to significantly enlarged  $E_a^{app}$  values of both the catalysts ( $> 110 \text{ kJ/mol}$ ). The relatively high energy barrier was caused by the competitive adsorption of water and propane over the available reactive sites, which inhibited propane activation — the kinetically relevant step for propane combustion [29,37,49]. Consequently, when 5 vol%  $H_2O$  was introduced into the feedstock, the catalysts exhibited sixfold lowered  $r_{C_3H_8}$  values (Fig. 3a and Table 3) and obviously increased propane light-off temperatures (Fig. 3b and Table 3). It is noteworthy that, the inhibition effects of moisture on the performance of catalysts were reversible. Both the catalysts fully recovered their initial activity once the water was removed from the atmosphere (Fig. S3a).

**Table 2**  
Quantitative summary of the  $C_3H_8$ -TPR/TPO and soot-TPR/TPO results.

Sample	$C_3H_8$ -TPR		$C_3H_8$ -TPO	soot-TPR		soot-TPO
	Total $CO_2$ generation (mmol/g) <sup>a</sup>	Ignition temperature (°C) <sup>b</sup>	Ignition temperature (°C) <sup>b</sup>	Total $CO_2$ generation (mmol/g) <sup>a</sup>	Ignition temperature (°C) <sup>b</sup>	Ignition temperature (°C) <sup>b</sup>
$CeO_2$	0.18	246	246	0.41	50	50
$Pr_6O_{11}$	0.63	246	246	1.77	50	50

<sup>a</sup>  $CO_2$  composed  $> 95\%$  of the total  $CO_x$  production in the TPR/TPO tests.

<sup>b</sup> At which the propane/soot  $\rightarrow CO_2$  conversion started.

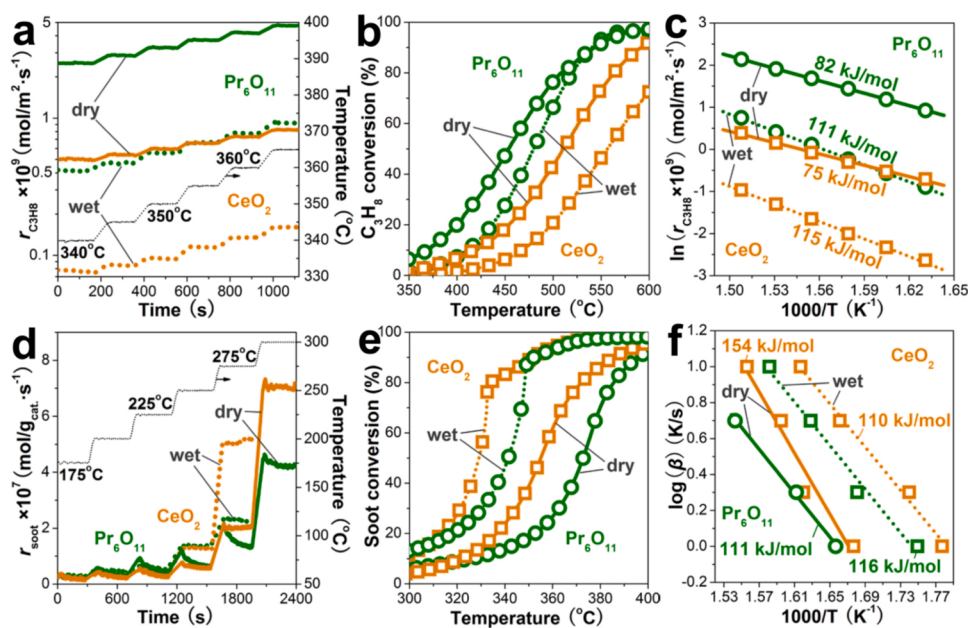


**Fig. 3.** The activities of CeO<sub>2</sub> and Pr<sub>6</sub>O<sub>11</sub> for (a, b, c) propane under 800 ppm C<sub>3</sub>H<sub>8</sub>/5% O<sub>2</sub>/N<sub>2</sub> (100 mg catalyst) and (d, e, f) soot combustion under 5% O<sub>2</sub>/N<sub>2</sub> (100 mg catalyst + 10 mg soot in the “tight” contact mode), with or without 5 vol% H<sub>2</sub>O (denoted as “dry” or “wet”). Gas flow rate = 500 mL/min, GHSV = 100,000 h<sup>-1</sup>. Catalytic performance obtained in the (a, d) isothermal and (b, e) TPO tests. (c) Arrhenius plots generated from the isothermal propane combustion tests ( $E_a^{app}$  marked beside the plots). (f) Ozawa plots obtained from the soot-TPO tests ( $E_a^{app}$  marked beside the plots).

**Table 3**  
The activities of CeO<sub>2</sub> and Pr<sub>6</sub>O<sub>11</sub> for propane and soot combustion.

Catalyst	Dry or wet <sup>a</sup>	propane combustion <sup>b</sup>			soot combustion <sup>b</sup>		
		$r_{C_3H_8}$ at 350°C (nmol <sub>C<sub>3</sub>H<sub>8</sub></sub> /m <sup>2</sup> ·s <sup>-1</sup> )	$T_{50}$ in C <sub>3</sub> H <sub>8</sub> -TPO (°C)	$E_a^{app}$ (kJ/mol)	$r_{soot}$ at 275°C (μmol <sub>soot</sub> /g <sub>cat.</sub> ·s <sup>-1</sup> )	$T_{50}$ in soot-TPO (°C)	$E_a^{app}$ (kJ/mol)
CeO <sub>2</sub>	Dry	0.60	511	75	0.20	354	154
	Wet	0.10	556	115	0.51	329	110
Pr <sub>6</sub> O <sub>11</sub>	Dry	3.27	453	82	0.13	373	111
	Wet	0.56	479	111	0.23	341	116

<sup>a</sup> Dry: reactions without water vapor. Wet: reactions with 5 vol% H<sub>2</sub>O in the atmosphere.

<sup>b</sup> All the reactions showed high CO<sub>2</sub> selectivity (CO<sub>2</sub>/CO<sub>x</sub> > 95%, see Fig. S3 for an example).

Since the soot particles cannot enter most of the micropores/mesopores that accessible for N<sub>2</sub>, the rate of soot combustion should be normalized by the number of catalyst-soot contact points instead of catalyst surface area [25,36]. As indicated in Section 3.1, the similar morphology of the CeO<sub>2</sub> and Pr<sub>6</sub>O<sub>11</sub> nanorods allowed them to contact with soot in nearly identical manners (Fig. 1 and S1). Therefore, the  $r_{soot}$  values (mol<sub>soot</sub>/g<sub>cat.</sub>·s<sup>-1</sup>) of these catalysts could be used directly to compare their intrinsic activity [24]. As shown in Fig. 3d, Pr<sub>6</sub>O<sub>11</sub> experienced severe deactivation with time on stream, especially at 200–275°C. Since the lattice oxygen in praseodymia represented the dominant reactive phase in this temperature range (Fig. 2d), it is suggested that the redox cycle was not closed over this sample (which will be evidenced in Section 3.5). In contrast, CeO<sub>2</sub> exhibited marginal deactivation at ≤ 250°C and only slightly lower  $r_{soot}$  values than Pr<sub>6</sub>O<sub>11</sub> at these temperatures. Moreover, after a sharp activation at elevated temperatures, CeO<sub>2</sub> showed a  $r_{soot}(275^\circ\text{C})$  1.5 times larger and a  $T_{50}$  19°C lower than those of Pr<sub>6</sub>O<sub>11</sub> (Fig. 3d, 3e and Table 3). Such an activity sequence ( $r_{soot,CeO_2} \geq r_{soot,Pr_6O_{11}}$ ) deviated from the soot consumption in the soot-TPR tests (Fig. 2d and 2f), implying the dynamic involvement of reactive phases other than lattice oxygen (e.g., O<sub>x</sub><sup>n</sup>) in CeO<sub>2</sub> [19–25]. The apparent activation energy ( $E_a^{app}$ ) values for the CeO<sub>2</sub> and Pr<sub>6</sub>O<sub>11</sub> catalyzed reactions were estimated by the Ozawa method (Fig. 3f). According to the results obtained by Krishna et al. [18], the  $E_a^{app}$  of the CeO<sub>2</sub>-catalyzed reaction (154 kJ/mol) was close to that of the un-catalyzed soot combustion (~150 kJ/mol), both of which were limited by the chemisorption of spillover oxygen species on carbon sites. These results indicated that the role of CeO<sub>2</sub> was to produce adsorbed O<sub>x</sub><sup>n</sup> species instead of incorporating them into the carbon framework of

soot [22–25]. In contrast, the direct involvement of Pr<sub>6</sub>O<sub>11</sub> lattice oxygen ( $2Pr^{4+}-O^{2-} + C \rightarrow 2Pr^{3+}-V_O + CO_2$ ) changed this superficial oxygen-dominated mechanism, overcame the barrier induced by oxygen (O<sub>x</sub><sup>n</sup>) chemisorption, and thereby led to a remarkably lowered  $E_a^{app}$  (111 kJ/mol).

Different from propane, the solid soot particles do not “adsorb” on the catalyst sites. Therefore, no inhibition effects could be caused by the adsorption of water on the catalysts. On the contrary, the water-derived oxygen species (e.g. hydroxyls) on catalyst surface accelerated the reactions by reacting with soot directly [24,50], which brought the  $E_a^{app}$  values of CeO<sub>2</sub> and Pr<sub>6</sub>O<sub>11</sub> to the same level (110–116 kJ/mol, Fig. 3f and Table 3). In the case of Pr<sub>6</sub>O<sub>11</sub>, these water-derived oxygen species became significantly reactive for soot oxidation at ≥ 250°C, which lightened the load of the lattice oxygen and prevented the time-on-stream deactivation of this sample (Fig. 3d). It is also noteworthy that, CeO<sub>2</sub> achieved obviously more water-induced activity bonus than did Pr<sub>6</sub>O<sub>11</sub> at ≥ 275°C (Fig. 3d). Such a difference implied that the reaction between H<sub>2</sub>O and CeO<sub>2</sub>-derived O<sub>x</sub><sup>n</sup> gave rise to hydrogen-containing oxidants besides hydroxyls — probably hydroperoxyls ( $H_2O^* + O_2^* \rightarrow ^*OOH + ^*OH$ ), which provided extra reactive phases for soot combustion. The water-induced promotion effects extended to the non-kinetic regime, decreased the  $T_{50}$  values of both the catalysts by ~30°C (Fig. 3e) and were reversible. After removing water from the reaction atmosphere (Fig. S3b), the catalysts restored their initial performance with the depletion of the water-derived oxidizing phases (e.g., hydroxyls and hydroperoxyls).

### 3.4. DRIFTS study of propane activation

In order to unveil the catalyst-induced propane activation — the rate-determining step for propane catalytic combustion in oxidizing conditions [29,37,49], DRIFT spectra of propane chemisorption were collected at temperatures ( $\leq 100^\circ\text{C}$ ) significantly lower than the reaction temperatures ( $\geq 246^\circ\text{C}$ , Table 2) to slow down the evolution of the kinetically-relevant surface intermediates and allow their detection [3]. As shown in Fig. 4 and S4, the bands between  $3000$  and  $2850\text{ cm}^{-1}$  originated from C-H stretch modes of chemisorbed propane that are nearly unconstrained by the surface (denoted as “free”, i.e., near gas-phase frequencies), while the red-shifted bands at  $2600$ – $2540\text{ cm}^{-1}$  should be attributed to the “soft” C-H stretch modes of propane  $\sigma$ -complexes on  $\text{CeO}_2$  or  $\text{Pr}_6\text{O}_{11}$  (Fig. S4) [51,52]. Specifically, for the propane covalently bonded with the coordinatively unsaturated  $\text{Ce}_{\text{cus}}$  or  $\text{Pr}_{\text{cus}}$  atoms, both the donation (propane bonding  $\sigma$  orbitals  $\rightarrow$  empty Ce/Pr  $f$  states) and backdonation (filled Ce/Pr  $f$  states  $\rightarrow$  propane antibonding  $\sigma^*$  orbitals) interactions softened the metal-coordinated C-H bonds and facilitated their scission [53]. Due to the smaller electrochemical reduction potential of  $\text{Ce}^{4+}/\text{Ce}^{3+}$  (1.74 eV) than that of  $\text{Pr}^{4+}/\text{Pr}^{3+}$  (3.2 eV), the donation-backdonation processes went more smoothly and gave rise to more propane  $\sigma$ -complexes with “soft” C-H bonds on  $\text{CeO}_2$  than on  $\text{Pr}_6\text{O}_{11}$  (see the bands at  $2600$ – $2540\text{ cm}^{-1}$  in Fig. 4). As a result,  $\text{CeO}_2$  exhibited lower  $E_a^{\text{app}}$  values than did  $\text{Pr}_6\text{O}_{11}$  for propane combustion (Fig. 3c). At elevated temperatures, the C-H stretch band at  $2596\text{ cm}^{-1}$  decreased while the one at  $2542\text{ cm}^{-1}$  intensified (Fig. 4a), indicating the evolution of adsorbed propane configurations on  $\text{CeO}_2$  ( $\text{CH}_3\text{CH}_2\text{CH}_3\text{-Ce}_{\text{cus}} \rightarrow (\text{CH}_3)_2\text{CH}_2\text{-Ce}_{\text{cus}}$ ) before converting into propyl radicals [52].

Although the adsorbed  $\text{O}_x^{\text{n-}}$  species were reportedly reactive for alkane activation and decomposition even at room temperature [7,8], the bands of the activated propane  $\sigma$ -complexes changed little after introducing gaseous  $\text{O}_2$  during the propane adsorption process (Fig. 4). It is therefore reconfirmed that superficial  $\text{O}_x^{\text{n-}}$  species played a much less important role than did interfacial lattice oxygen in propane catalytic combustion. Within the framework of a precursor-mediated propane combustion mechanism [53], the rapid formation and/or slow decomposition of the activated propane  $\sigma$ -complexes on  $\text{CeO}_2$  (Fig. 4) indicated that during reactions, a large extent of the  $\text{CeO}_2$  free active sites may be covered by the kinetically-relevant intermediates, leading to a low  $\theta_*$  value. In contrast, due to the weak propane activation and the unstable lattice oxygen over  $\text{Pr}_6\text{O}_{11}$  (Fig. 2), this sample should exhibit relatively high  $\theta_*$  values at reaction temperatures. These results were in harmony with the data in Fig. 3c and Table 3, which well explained the kinetic regime shift behind the compensation effect [47,48].

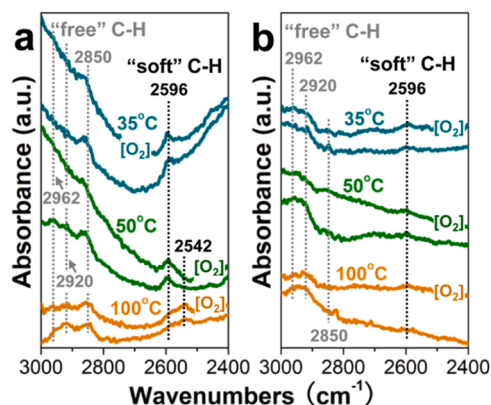


Fig. 4. DRIFT spectra of propane adsorption at 35, 50 and  $100^\circ\text{C}$  over (a)  $\text{CeO}_2$  and (b)  $\text{Pr}_6\text{O}_{11}$ . Adsorption in 800 ppm  $\text{C}_3\text{H}_8/\text{N}_2$  or 800 ppm  $\text{C}_3\text{H}_8/5\%\text{ O}_2/\text{N}_2$  (denoted with  $[\text{O}_2]$ ) for 30 min, followed by  $\text{N}_2$  purging for another 30 min.

### 3.5. Reconstruction of the catalysts during reactions

Surface reconstruction, especially the dynamic formation/annihilation of interfacial defects makes up the key steps in Mars-van Krevelen-type reactions. Permanent changes in catalyst structure/chemical states may occur once the consumption and replenishment of oxygen are not balanced. As shown in Fig. 5a and Table 4, the spent  $\text{CeO}_2$  catalyst showed no XPS-detectable changes in chemical states, indicating its overall stable surface structure originating from the fast oxygen vacancy refilling than ceria reduction [54]. With the assistance of EPR — a technique highly sensitive to the presence of vacancies and superficial oxygen species [42,43], the adsorbed  $\text{O}_2^-$  over  $\text{CeO}_2$  was confirmed to be consumed or removed during both the reactions, while oxygen vacancies ( $\text{V}_\text{O}$ ) were observed only after soot combustion (Fig. 5b). These defective sites were most likely located at the catalyst-soot contact points [22,23], which counted for only a fraction of the total ceria surface defects and could not be revealed by XPS [55]. As a milder reductant than soot (Table 2), propane led to certain degree of  $\text{CeO}_2$  reduction (see the  $\text{Ce}^{3+}$  signals in Fig. 5b) — perhaps through the propane  $\rightarrow \text{Ce}_{\text{cus}}$  donation interaction [53], but left a closed redox cycle for the spent  $\text{CeO}_2$  catalyst.

Similar to the case of  $\text{CeO}_2$ , the surface structure and  $\text{Pr}^{3+}/\text{Pr}^{4+}$  values of  $\text{Pr}_6\text{O}_{11}$  remained intact after reacting with  $\text{C}_3\text{H}_8 + \text{O}_2$  (Fig. 5c and Table 4). In contrast, the reaction with soot +  $\text{O}_2$  led to significant weakened  $\text{Pr}^{4+}$ -related XPS signals (Fig. 5c) [56,57] and the emergence of singly ionized  $\text{V}_\text{O}$ -related EPR signals ( $g = 1.997$ , Fig. 5d), suggesting the interfacial lattice oxygen of  $\text{Pr}_6\text{O}_{11}$  was deeply involved in this reaction but could not be replenished in time. Without the participation of external oxidants (e.g. water-derived hydroxyls), such unsustainable consumption of the reactive phases would lead to catalyst deactivation with time on stream, as evidenced by the isothermal soot oxidation results under the “dry” conditions (Fig. 3d).

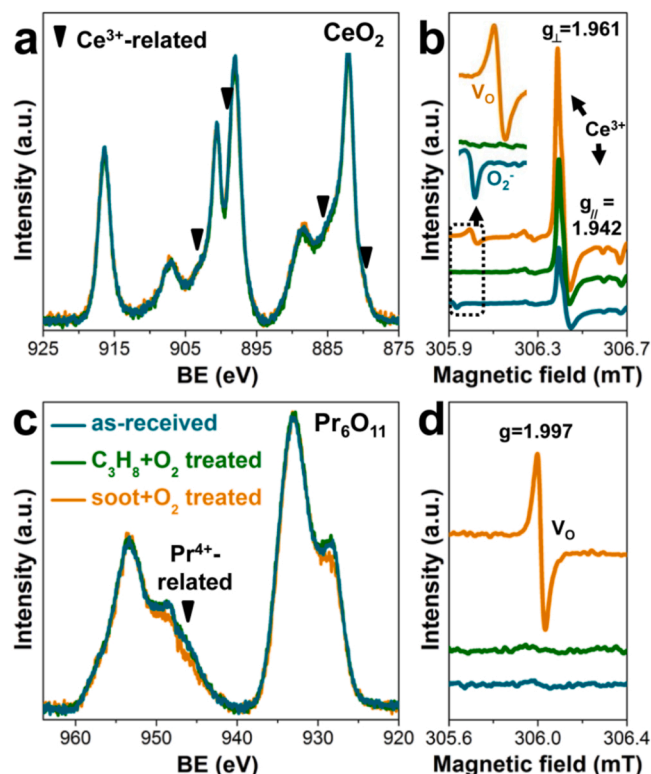


Fig. 5. (a,c) XPS and (b,d) EPR spectra of (a,b)  $\text{CeO}_2$  and (c,d)  $\text{Pr}_6\text{O}_{11}$  before or after reacting with propane (800 ppm  $\text{C}_3\text{H}_8/5\%\text{ O}_2/\text{N}_2$ ) at  $375^\circ\text{C}$  or soot (catalyst/soot = 10/1 in the “tight” contact mode,  $5\%\text{ O}_2/\text{N}_2$ ) at  $300^\circ\text{C}$  for 30 min. All the figures share the same legend.



**Table 4**

Chemical state information of CeO<sub>2</sub> and Pr<sub>6</sub>O<sub>11</sub> before or after reacting with C<sub>3</sub>H<sub>8</sub> + O<sub>2</sub> at 375 °C or soot + O<sub>2</sub> at 300 °C for 30 min (deconvolution details shown in Fig. S5).

	As-received	After reacting with C <sub>3</sub> H <sub>8</sub> + O <sub>2</sub>	After reacting with soot + O <sub>2</sub>
Ce <sup>3+</sup> /(Ce <sup>3+</sup> +Ce <sup>4+</sup> ) in CeO <sub>2</sub>	28.4%	28.5%	28.4%
Pr <sup>3+</sup> /(Pr <sup>3+</sup> +Pr <sup>4+</sup> ) in Pr <sub>6</sub> O <sub>11</sub>	47.3%	47.3%	53.0%

### 3.6. Reaction mechanisms for C<sub>3</sub>H<sub>8</sub>/soot combustion over the catalysts

Reaction models can be built based on the above results. As shown in Fig. 6a, the catalytic combustion of propane over CeO<sub>2</sub> and Pr<sub>6</sub>O<sub>11</sub> followed closed Mars-van Krevelen (redox) cycles, in which the interfacial lattice oxygen represented the dominant reactive phases while the superficial O<sub>x</sub><sup>n-</sup> played negligible roles. Specifically, propane chemisorbed as activated σ-complexes on rows of Ce<sub>cus</sub> or Pr<sub>cus</sub> atoms, the hydrogen in its softened C-H bonds (especially the one on the second carbon of propane, Fig. 4a) was then accepted by adjacent bridging oxygen atoms (O<sub>br</sub>) [3,4,37,53]. After regenerating via HO<sub>br</sub> recombination, these O<sub>br</sub> sites led to exclusive dehydrogenation of the propyl radicals and ultimately converted them into CO<sub>2</sub> [49]. In comparison with CeO<sub>2</sub>, Pr<sub>6</sub>O<sub>11</sub> exhibited lower lattice oxygen stability (Fig. 2 and Table 2), resulting in its faster oxygen-C<sub>3</sub>H<sub>8</sub> incorporation, higher θ\* values, larger pre-exponential factor and thereby higher propane combustion rates (Fig. 3 and Table 3) [47,48].

Due to the solid nature of soot, there is no “adsorption” process during its catalytic combustion. Instead, the contact points between catalysts and soot are the only effective venues for catalyst-soot oxygen transfer and catalyzed soot oxidation [17,25]. At the beginning of the reaction, for both CeO<sub>2</sub> and Pr<sub>6</sub>O<sub>11</sub>, plenty of lattice oxygen (plus some O<sub>x</sub><sup>n-</sup> in the case of CeO<sub>2</sub>) was located at these contact points, which led to soot ignition at relatively low temperatures (i.e., 50 °C, see Fig. 2). As the reaction proceeded, the strongly reducing soot led to excessive consumption of the interfacial lattice oxygen and gave rise to surface defective sites (i.e., Ce<sup>3+</sup>-V<sub>O</sub> and Pr<sup>3+</sup>-V<sub>O</sub>). For the CeO<sub>2</sub> sample, its further interaction with gaseous O<sub>2</sub> produced superficial O<sub>x</sub><sup>n-</sup> species (Ce<sup>3+</sup>-V<sub>O</sub> + O<sub>2</sub> → Ce<sup>4+</sup>-O<sub>x</sub><sup>n-</sup>) [5,6]. As shown in Fig. 6b, these electrophilic oxygen species were continuously consumed by soot and regenerated at the soot-Ce<sup>3+</sup>-V<sub>O</sub> interface [55], which worked as the principal oxidizing agents for CeO<sub>2</sub>-catalyzed soot combustion especially at elevated temperatures [19,24]. These results agreed well with the in situ XPS and Raman data obtained by the group of Llorca [22,23], demonstrating a ceria reconstruction-mediated soot oxidation mechanism. Notably, since all these tests were performed with excessive gaseous O<sub>2</sub> (5%), the formation of ceria defective sites (Ce<sup>3+</sup>-V<sub>O</sub>) was suppressed to a large extent (Fig. 5a). Therefore, the deactivation caused by V<sub>O</sub>-trapping (O<sub>x</sub><sup>n-</sup> + V<sub>O</sub> → V<sub>O</sub>-O<sub>x</sub><sup>n-</sup>) and O<sub>x</sub><sup>n-</sup> annihilation (O<sub>x</sub><sup>n-</sup> → O<sup>2-</sup>) — which occurred commonly in CeO<sub>2</sub>-catalyzed soot combustion reactions under oxygen-lacking atmospheres (e.g., simulated working conditions of gasoline particulate filters) [25,28] — were not obvious in this work (Fig. 3d). Different from case of CeO<sub>2</sub>, the high electrochemical reduction potential of Pr<sup>4+</sup>/Pr<sup>3+</sup> (3.2 eV) hampered the generation of O<sub>x</sub><sup>n-</sup> over Pr<sub>6</sub>O<sub>11</sub> (Pr<sup>3+</sup>-V<sub>O</sub> + O<sub>2</sub> → Pr<sup>4+</sup>-O<sub>x</sub><sup>n-</sup>, see Fig. 2 for details) [33,34]. As a consequence, this sample always followed a typical redox mechanism to oxidize soot. This reaction pathway exhibited relatively low activation energy (Fig. 3f) and was quite efficient at an initial stage (Fig. 3d). However, since the redox cycles for soot catalytic combustion were not closed, such a pathway became gradually ineffective with the draining of the Pr<sub>6</sub>O<sub>11</sub> interfacial lattice oxygen (Fig. 3d and 3e).

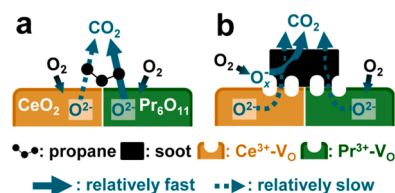


**Fig. 6.** Reaction mechanisms of (a) propane and (b) soot combustion over CeO<sub>2</sub> and Pr<sub>6</sub>O<sub>11</sub>.

### 4. Conclusions

In this study, CeO<sub>2</sub> and Pr<sub>6</sub>O<sub>11</sub> nanorods with similar morphology and structure were synthesized. Due to the distinct electrochemical reduction potential of Ce<sup>4+</sup>/Ce<sup>3+</sup> (1.74 eV) and Pr<sup>4+</sup>/Pr<sup>3+</sup> (3.2 eV), these catalysts preferred the generation/utilization of superficial O<sub>x</sub><sup>n-</sup> and interfacial lattice oxygen, respectively. By comparing their catalytic performance for propane and soot combustion under lean-burn conditions, several conclusions can be drawn as:

- (1) The catalytic combustion of propane followed a typical Mars-van Krevelen mechanism, in which the lattice oxygen in catalysts played crucial roles. Pr<sub>6</sub>O<sub>11</sub> with higher lattice oxygen mobility exhibited faster propane oxidation rate than did CeO<sub>2</sub>.
- (2) The ignition of soot followed a Mars-van Krevelen mechanism with open redox cycles. In the proceeding reaction progress, the O<sub>x</sub><sup>n-</sup> species induced by surface defective sites worked as the key reactive phases of CeO<sub>2</sub>, while Pr<sub>6</sub>O<sub>11</sub> with poor O<sub>x</sub><sup>n-</sup> replenishment ability deactivated gradually with the draining of its interfacial lattice oxygen.

Based on the above investigation, the dominance of superficial O<sub>x</sub><sup>n-</sup> and interfacial lattice oxygen can be roughly estimated by running temperate-programmed oxidation tests over model CeO<sub>2</sub> and Pr<sub>6</sub>O<sub>11</sub> catalysts. Although the thus-obtained results were subject to the specific reaction conditions applied herein, and could not give the exact share of superficial and interfacial mechanisms in the catalytic combustion reactions, they provided a simple strategy to distinguish the dominant reactive phases over oxidation catalysts consisting of reducible metal oxides.

### CRediT authorship contribution statement

Xuezan Mao and Shuran Liu: performed the experiments. Wei Liu: helped manuscript writing and editing. Xiaodong Wu: co-directed the project and co-wrote the manuscript. Shuang Liu: directed the project, conceived and designed the experiments, wrote, reviewed and edited the manuscript.

### Declaration of Competing Interest

The authors declare that they have no known competing financial interests or personal relationships that could have appeared to influence the work reported in this paper.

### Acknowledgements

The authors would like to acknowledge the financial support from projects of the National Key R&D Program of China (2017YFC0211102), the National Natural Science Foundation of China (22076176), the Natural Science Foundation of Shandong Province (ZR2021YQ14), the Youth Innovation Plan of Shandong Province (2019KJ001) and the Fundamental Research Funds for the Central Universities (202141008, 202042002, 202061047).

## Appendix A. Supporting information

Supplementary data associated with this article can be found in the online version at [doi:10.1016/j.apcatb.2022.121331](https://doi.org/10.1016/j.apcatb.2022.121331).

## References

- [1] A. Bielanski, J. Haber, *Oxygen in Catalysis*, Marcel Dekker Inc., New York, 1991, pp. 1–466.
- [2] J. Paier, C. Penschke, J. Sauer, Oxygen defects and surface chemistry of ceria: quantum chemical studies compared to experiment, *Chem. Rev.* 113 (2013) 3949–3985.
- [3] G. Busca, E. Finocchio, V. Lorenzelli, G. Ramis, M. Baldi, IR studies on the activation of C–H hydrocarbon bonds on oxidation catalysts, *Catal. Today* 49 (1999) 453–465.
- [4] S. Kwon, P. Deshlahra, E. Iglesia, Reactivity and selectivity descriptors of dioxygen activation routes on metal oxides, *J. Catal.* 377 (2019) 692–710.
- [5] M. Huang, S. Fabris, Role of surface peroxo and superoxo species in the low-temperature oxygen buffering of ceria: density functional theory calculations, *Phys. Rev. B* 75 (2007), 081404.
- [6] G. Preda, A. Migani, K.M. Neyman, S.T. Bromley, F. Illas, G. Pacchioni, Formation of superoxide anions on ceria nanoparticles by interaction of molecular oxygen with  $\text{Ce}^{3+}$  sites, *J. Phys. Chem. C* 115 (2011) 5817–5822.
- [7] M. Anpo, G. Costentin, E. Giamello, H. Lauron-Pernot, Z. Sojka, Characterisation and reactivity of oxygen species at the surface of metal oxides, *J. Catal.* 393 (2021) 259–280.
- [8] K. Aika, J.H. Lunsford, Surface reactions of oxygen ions. 1. Dehydrogenation of alkanes by  $\text{O}^-$  on  $\text{MgO}$ , *J. Phys. Chem.* 81 (1977) 1393–1398.
- [9] M. Iwamoto, J.H. Lunsford, Surface reactions of oxygen ions. 5. Oxidation of alkanes and alkenes by  $\text{O}_2^-$  on  $\text{MgO}$ , *J. Phys. Chem.* 84 (1980) 3079–3084.
- [10] T. Tashiro, T. Ito, K. Toi, Reaction of methane with nitrous oxide over magnesium oxide at low temperatures, *J. Chem. Soc., Faraday Trans. 86* (1990) 1139–1146.
- [11] J. Haber, *Fundamentals of Hydrocarbon Oxidation*, in: G. Ertl, H. Knözinger, F. Schüth, J. Weitkamp (Eds.), *Handbook of Heterogeneous Catalysis*, Wiley-VCH Verlag GmbH & Co. KGaA, Weinheim, 2008, pp. 3359–3384.
- [12] M.A. Banares, Supported Metal Oxide and Other Catalysts for Ethane Conversion: A review, *Catal. Today* 51 (1999) 319–348.
- [13] G. Busca, Infrared studies of the reactive adsorption of organic molecules over metal oxides and of the mechanisms of their heterogeneously-catalyzed oxidation, *Catal. Today* 27 (1996) 457–496.
- [14] R. Burch, M.J. Hayes, C–H bond activation in hydrocarbon oxidation on solid catalysts, *J. Mol. Catal. A* 100 (1995) 13–33.
- [15] A. Bueno-López, K. Krishna, M. Makkee, J.A. Moulijn, Enhanced soot oxidation by lattice oxygen via  $\text{La}^{3+}$ -doped  $\text{CeO}_2$ , *J. Catal.* 230 (2005) 237–248.
- [16] A. Bueno-López, K. Krishna, M. Makkee, J.A. Moulijn, Active oxygen from  $\text{CeO}_2$  and its role in catalysed soot oxidation, *Catal. Lett.* 99 (2005) 203–205.
- [17] S.B. Simonsen, S. Dahl, E. Johnson, S. Helveg, Ceria-catalyzed soot oxidation studied by environmental transmission electron microscopy, *J. Catal.* 255 (2008) 1–5.
- [18] K. Krishna, A. Bueno-López, M. Makkee, J.A. Moulijn, Potential rare earth modified  $\text{CeO}_2$  catalysts for soot oxidation I. Characterisation and catalytic activity with  $\text{O}_2$ , *Appl. Catal. B* 75 (2007) 189–200.
- [19] M. Machida, Y. Murata, K. Kishikawa, D. Zhang, K. Ikeue, On the reasons for high activity of  $\text{CeO}_2$  catalyst for soot oxidation, *Chem. Mater.* 20 (2008) 4489–4494.
- [20] K. Yamazaki, T. Kayama, F. Dong, H. Shinjoh, A mechanistic study on soot oxidation over  $\text{CeO}_2$ –Ag catalyst with ‘rice-ball’ morphology, *J. Catal.* 282 (2011) 289–298.
- [21] K. Yamazaki, Y. Sakakibara, F. Dong, H. Shinjoh, The remote oxidation of soot separated by ash deposits via silver–ceria composite catalysts, *Appl. Catal. A* 476 (2014) 113–120.
- [22] L. Soler, A. Casanovas, C. Escudero, V. Pérez-Dieste, E. Aneggi, A. Trovarelli, J. Llorca, Ambient pressure photoemission spectroscopy reveals the mechanism of carbon soot oxidation in ceria-based catalysts, *ChemCatChem* 8 (2016) 2748–2751.
- [23] X. Garcia, L. Soler, A. Casanovas, C. Escudero, J. Llorca, X-ray photoelectron and raman spectroscopy of nanostructured ceria in soot oxidation under operando conditions, *Carbon* 178 (2021) 164–180.
- [24] H. Wang, S. Luo, M. Zhang, W. Liu, X. Wu, S. Liu, Roles of oxygen vacancy and  $\text{O}_x^-$  in oxidation reactions over  $\text{CeO}_2$  and Ag/ $\text{CeO}_2$  nanorod model catalysts, *J. Catal.* 368 (2018) 365–378.
- [25] S. Liu, X. Wu, W. Liu, W. Chen, R. Ran, M. Li, D. Weng, Soot oxidation over  $\text{CeO}_2$  and Ag/ $\text{CeO}_2$ : Factors determining the catalyst activity and stability during reaction, *J. Catal.* 337 (2016) 188–198.
- [26] A.H. Castro Neto, F. Guinea, N.M.R. Peres, K.S. Novoselov, A.K. Geim, The electronic properties of graphene, *Rev. Mod. Phys.* 81 (2009) 109–162.
- [27] A. Naseri, A.D. Sediako, F. Liu, M. Barati, R.D. Baker, M.J. Thomson, In-situ studies of  $\text{O}_2$  and  $\text{O}$  radical oxidation of carbon black using thermogravimetric analysis and environmental transmission electron microscopy, *Carbon* 156 (2020) 299–308.
- [28] S. Liu, X. Wu, J. Tang, P. Cui, X. Jiang, C. Chang, W. Liu, Y. Gao, M. Li, D. Weng, An exploration of soot oxidation over  $\text{CeO}_2$ – $\text{ZrO}_2$  nanocubes: Do more surface oxygen vacancies benefit the reaction? *Catal. Today* 281 (2017) 454–459.
- [29] K. Chen, A. Khodakov, J. Yang, A.T. Bell, E. Iglesia, Isotopic tracer and kinetic studies of oxidative dehydrogenation pathways on vanadium oxide catalysts, *J. Catal.* 186 (1999) 325–333.
- [30] D. Martin, D. Duprez, Mobility of surface species on oxides. 1. Isotopic exchange of  $^{18}\text{O}_2$  with  $^{16}\text{O}$  of  $\text{SiO}_2$ ,  $\text{Al}_2\text{O}_3$ ,  $\text{ZrO}_2$ ,  $\text{MgO}$ ,  $\text{CeO}_2$ , and  $\text{CeO}_2$ – $\text{Al}_2\text{O}_3$ . Activation by noble metals. correlation with oxide basicity, *J. Phys. Chem.* 100 (1996) 9429–9438.
- [31] F. Zasada, J. Janas, W. Piskorz, M. Gorczyńska, Z. Sojka, Total oxidation of lean methane over cobalt spinel nanocubes controlled by the self-adjusted redox state of the catalyst: Experimental and theoretical account for interplay between the langmuir-hinshelwood and mars-van krevelen mechanisms, *ACS Catal.* 7 (2017) 2853–2867.
- [32] J. Gryboś, M. Fedyna, P. Legutko, B. Leszczynski, J. Janas, A. Wach, J. Szlachetko, X. Yu, A. Kotarba, Z. Zhao, Z. Sojka, Mechanistic insights into oxygen dynamics in soot combustion over cryptomelane catalysts in tight and loose contact modes via  $^{18}\text{O}_2$ / $^{16}\text{O}_2$  isotopic variable composition measurements - a hot ring model of the catalyst operation, *ACS Catal.* 11 (2021) 9530–9546.
- [33] G. Niu, M.H. Zoellner, T. Schroeder, A. Schaefer, J. Jhang, V. Zielasek, M. Bäumer, H. Wilkens, J. Wollschläger, R. Olbrich, C. Lammers, M. Reichling, Controlling the physics and chemistry of binary and ternary praseodymium and cerium oxide systems, *Phys. Chem. Chem. Phys.* 17 (2015) 24513–24540.
- [34] R.J. Gorte, Ceria in catalysis: From automotive applications to the water–gas shift reaction, *AIChE J.* 56 (2010) 1126–1135.
- [35] A. Yang, H. Zhu, Y. Li, M. Cargnello, Support acidity improves Pt activity in propane combustion in the presence of steam by reducing water coverage on the active sites, *ACS Catal.* 11 (2021) 6672–6683.
- [36] H. Liang, B. Jin, M. Li, X. Yuan, J. Wan, W. Liu, S. Liu, Highly reactive and thermally stable Ag/YSZ catalysts with macroporous fiber-like morphology for soot combustion, *Appl. Catal. B* 294 (2021), 120271.
- [37] E. Finocchio, G. Busca, V. Lorenzelli, R.J. Willey, The activation of hydrocarbon C–H bonds over transition metal oxide catalysts: a FTIR study of hydrocarbon catalytic combustion over  $\text{MgCr}_2\text{O}_4$ , *J. Catal.* 151 (1995) 204–215.
- [38] S. Chretien, H. Metiu, Acid-base interaction and its role in alkane dissociative chemisorption on oxide surfaces, *J. Phys. Chem. C* 118 (2014) 27336–27342.
- [39] S. Liu, X. Wu, D. Weng, M. Li, R. Ran, Roles of acid sites on Pt/H-ZSM5 catalyst in catalytic oxidation of diesel soot, *ACS Catal.* 5 (2015) 909–919.
- [40] S. Liu, X. Wu, H. Luo, D. Weng, R. Ran, Pt/Zelite catalysts for soot oxidation: influence of hydrothermal aging, *J. Phys. Chem. C* 119 (2015) 17218–17227.
- [41] M. Tamura, K. Shimizu, A. Satsuma, Comprehensive IR study on acid/base properties of metal oxides, *Appl. Catal. A* 433–434 (2012) 135–145.
- [42] R.C.R. Neto, M. Schmal, Synthesis of  $\text{CeO}_2$  and  $\text{CeZrO}_2$  mixed oxide nanostructured catalysts for the iso-syntheses reaction, *Appl. Catal. A* 450 (2013) 131–142.
- [43] J. Soria, A. Martínez-Arias, J.C. Conesa, Spectroscopic study of oxygen adsorption as a method to study surface defects on  $\text{CeO}_2$ , *J. Chem. Soc., Faraday Trans. 91* (1995) 1669–1678.
- [44] Z. Wu, M. Li, J. Howe, H.M. Meyer III, S.H. Overbury, Probing defect sites on  $\text{CeO}_2$  nanocrystals with well-defined surface planes by raman spectroscopy and  $\text{O}_2$  adsorption, *Langmuir* 26 (2010) 16595–16606.
- [45] Y. Takasu, M. Matsui, H. Tamura, S. Kawamura, Y. Matsuda, I. Toyoshima, Temperature-programmed desorption on the unstable lattice oxygen of praseodymium oxide, *J. Catal.* 69 (1981) 51–57.
- [46] A.V. Vishnyakov, I.A. Korshunova, V.E. Kochurikhin, L.S. Sal’nikova, Catalytic activity of rare earth oxides in flameless methane combustion, *Kinet. Catal.* 51 (2010) 273–278.
- [47] T. Bligaard, K. Honkala, A. Logadottir, J.K. Nørskov, On the compensation effect in heterogeneous catalysis, *J. Phys. Chem. B* 107 (2003) 9325–9331.
- [48] D. Teschner, G. Novell-Leruth, R. Farra, A. Knop-Gericke, R. Schlögl, L. Szentmiklósi, M.G. Hevia, H. Soerijanto, R. Schomäcker, J. Pérez-Ramírez, N. López, In Situ surface coverage analysis of  $\text{RuO}_2$ -catalysed HCl oxidation reveals the entropic origin of compensation in heterogeneous catalysis, *Nat. Chem.* 4 (2012) 739–745.
- [49] M.D. Krcha, M.J. Janik, Catalytic propane reforming mechanism over Mn-doped  $\text{CeO}_2$  (111), *Surf. Sci.* 640 (2015) 119–126.
- [50] W. Yang, Y. Wang, H. Wang, Y. Zhang, Y. Peng, J. Li, Water accelerates and directly participates soot oxidation: an isotopic study, *Appl. Catal. B* 302 (2022), 120837.
- [51] T. Koitaya, J. Yoshinobu, The quantum nature of C–H...metal interaction: vibrational spectra and kinetic and geometric isotope effects of adsorbed cyclohexane, *Chem. Rec.* 14 (2014) 848–856.
- [52] F. Zhang, L. Pan, J. Choi, V. Mehar, J.T. Diulus, A. Asthagiri, J.F. Weaver, Propane  $\sigma$ -complexes on  $\text{PdO}(101)$ : spectroscopic evidence of the selective coordination and activation of primary C–H bonds, *Angew. Chem. Int. Ed.* 54 (2015) 13907–13911.
- [53] R. Martin, M. Kim, A. Asthagiri, J.F. Weaver, Alkane activation and oxidation on late-transition-metal oxides: challenges and opportunities, *ACS Catal.* 11 (2021) 4682–4703.
- [54] R. Kopelent, J.A. Bokhoven, J. Szlachetko, J. Edebeli, C. Paun, M. Nachttegaal, O. V. Safonova, Catalytically active and spectator  $\text{Ce}^{3+}$  in ceria-supported metal catalysts, *Angew. Chem. Int. Ed.* 54 (2015) 8728–8731.



- [55] M. Zhang, B. Jin, Y. Liu, W. Liu, D. Weng, X. Wu, S. Liu, Ozone activated Ag/CeO<sub>2</sub> catalysts for soot combustion: the surface and structural influences, *Chem. Eng. J.* 375 (2019), 121961.
- [56] H. Borchert, Y.V. Frolova, V.V. Kaichev, I.P. Prosvirin, G.M. Alikina, A. I. Lukashovich, V.I. Zaikovskii, E.M. Moroz, S.N. Trukhan, V.P. Ivanov, E. A. Paukshtis, V.I. Bukhtiyarov, V.A. Sadykov, Electronic and chemical properties of nanostructured cerium dioxide doped with praseodymium, *J. Phys. Chem. B* 109 (2005) 5728–5738.
- [57] A. Schaefer, S. Gevers, V. Zielasek, T. Schroeder, J. Falta, J. Wollschläger, M. Bäumer, Photoemission study of praseodymium in its highest oxidation state: the necessity of in situ plasma treatment, *J. Chem. Phys.* 134 (2011), 054701.